Accurate Small-Signal Equivalent Circuit Modelling of Resonant Tunneling Diodes to 110 GHz

Razvan Morariu, Jue Wang, Andrei Catalin Cornescu, Abdullah Al-Khalidi, Afesomeh Ofiare, José M. L. Figueiredo, *Member, IEEE,* and Edward Wasige, *Member IEEE*

***Abstract*— This paper presents a novel, on-wafer de-embedding technique for the accurate small-signal equivalent circuit modelling of resonant tunneling diodes (RTDs). The approach is applicable to stabilised RTDs, and so enables the modelling of the negative differential resistance (NDR) region of the device's current-voltage (*I-V*) characteristics. Further, a novel quasi-analytical procedure to determine all the equivalent circuit elements from the de-embedded S-parameter data is developed. Extraction results for a 10 x 10 μm^2 stabilised, low-current density RTD at different bias points show excellent fits between modelled and measured S-parameters up to 110 GHz.**

***Index Terms*— Bias oscillations, experimental modelling, parameter extraction, Resonant tunneling diode (RTD), small-signal equivalent circuit.**

I. Introduction

Terahertz (THz) radiation, which has an electromagnetic spectrum that lies between millimetre-waves and infrared light, has become, over the last decade, a primary research interest in the fields of medical diagnostics, security imaging and wireless communications [1]. The resonant tunnelling diode (RTD) is a quantum-well structure, which exhibits negative differential resistance (NDR) that extends into the THz range, thus making it one of the target candidates for such applications. There is intense on-going research on this device technology to realise compact and coherent THz sources [2]-[5]. Fundamental frequency oscillations at around 2 THz have recently been obtained from RTD oscillators [6]. Compared to other electronic device technologies that may be used in the 0.1 – 1 THz band such as transistors, Gunn diodes, etc., the RTD exhibits the largest bandwidth (for a given device size), requires simple circuitry, is compact, and consumes low power [7]. Recently, high performance RTD based THz short range multi-gigabit wireless links [8]-[10] and imaging applications have been demonstrated [11]. Thus, the accurate modelling of RTDs to support reliable THz circuit design is of paramount importance.

The key device operation region of interest, which gives the RTD its performance advantages over competing technologies (for the THz band), is its negative differential resistance (NDR) region. Without stabilisation circuitry, the device bursts into oscillations when biased in the NDR, rendering the characterisation of this region difficult [12], [13]. The common approach to achieve bias stability is to use a suitable shunt resistance connected across the RTD, chosen such that the combined conductance is positive. Using this approach, the device *I-V* characteristic within the NDR can be determined indirectly [14], [15]. This approach has also been used once for the RF characterisation of the NDR region, but no details about the de-embedding of the stabilising resistor were provided [16]. The increased complexity of the resistor model at high frequency to account for parasitic effects such as self-inductance together with the RTD makes this approach difficult to implement at millimeter-waves

Another approach to characterise the NDR region is to use physically small devices, usually sub-micron device dimensions [17], since for such devices the negative differential conductance is also small making them stable in a conventional measurement setup, e.g. when characterised by a vector network analyser in the typical 50-Ω system impedance. This approach is, however, only applicable to low peak current density RTDs, so less than about 100 kA/cm^2 [18]. For high current density designs (>300 kA/cm^2), even small submicron devices remain unstable when biased in the NDR region and so must employ a stabilising resistance [19]. Therefore, the characterisation of the NDR region of such devices is usually not possible. Presently, RF characterisation of an RTD in its positive differential resistance (PDR) region is used to estimate its equivalent circuit elements in the NDR region [20], [21]. Even for a key parameter such as the device self-capacitance, its extraction is done at only a single frequency, 10 GHz [20], and so there is limited scope to validate the accuracy of this approach.

In this paper, we report a new approach to characterise the NDR regions of (stabilised) RTDs without limitations to device

Manuscript received xx, 2019. This work was supported in part by the European Commission through the iBROW and TERAPOD projects under grants 645369 and 761579, respectively It was also supported by the Engineering and Physical Sciences Research Council (EPSRC) through a PhD studentship to Razvan Morariu.

R. Morariu, J. Wang, A. C. Cornescu, A. Al-Khalidi, A. Ofiare, and E. Wasige are with the High Frequency Electronics Group, School of Engineering, University of Glasgow, Glasgow G12 8LT, U.K. (e-mail: r.morariu.1@research.gla.ac.uk).

J. M. L. Figueiredo is with the Department of Physics, Faculty of Sciences of the University of Lisbon, Portugal.

sizing or frequency. It uses a universal on-wafer bond-pad and shunt resistor de-embedding technique for reliable high frequency characterisation. Further, a quasi-analytical procedure to determine the RTD equivalent circuit elements is also developed. The new de-embedding and extraction procedure is applied to a 10 x 10 μm^2 AlAs–InGaAs–AlAs device stabilised with a 20 **Ω** shunt stabilisation resistor at different bias points.

The paper is organised as follows: Section II describes the procedure for de-embedding the shunt stabilisation resistor from S-parameter measurements, while section III provides details of the RTD epitaxial structure, its manufacturing including that of the shunt resistor and the measured RTD *I-V* characteristics. RF device and test-fixture characterisation and validation is described in Section IV, while the new parameter extraction of the RTD equivalent circuit elements is described in Section V. A comparison of the extracted element values with those determined using alternate methods to estimate the device parameters, in particular, those found on the basis of device physics, is given in Section VI. Conclusions are given in Section VII.

II. RF Analysis Of A Stabilised RTD

Fig. 1. shows an RTD with a shunt resistor for bias stabilisation connected across it. The stabilising resistor including the interconnections can be considered as a standard 2-port network as shown in Fig. 1. If the RTD has a reflection coefficient, Γ_{RTD}, and the stabilising network is described by its S-parameter matrix, then the input reflection coefficient Γ_{in} will be given by [22]:

$$\Gamma_{in} = S_{11} + \frac{S_{12}S_{21}\Gamma_{rtd}}{1-S_{22}\Gamma_{rtd}}. \quad (1)$$

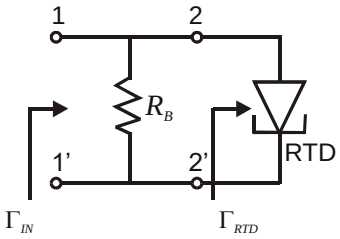

Fig. 1. RTD biased through a shunt resistor R_B, modelled as a 2-port network.

Re-arranging (1) gives the reflection coefficient of the RTD, Γ_{RTD}:

$$\Gamma_{rtd} = \frac{\Gamma_{in}-S_{11}}{\Gamma_{in}S_{22}-S_{11}S_{22}+S_{12}S_{21}}. \quad (2)$$

where S_{11}, S_{12}, S_{21}, and S_{22} are the S-parameters of the 2-port stabilising network. These S-parameters can be obtained by a two-port measurement of a fabricated auxiliary test structure, identical to the stabilised RTD but without the device under test (DUT).

III. RTD Device And Test-Fixture Fabrication

The RTD epitaxial wafer used in this work was grown by molecular beam epitaxy (MBE) by IQE Ltd on a semi-insulating InP substrate. The epitaxial layer structure consists of a 4.7 nm InGaAs quantum well (E_g = 0.75 eV) sandwiched between 2.5 nm thick AlAs barriers (E_g = 2.16 eV), forming a double barrier quantum well structure (DBQW). The structure is completed by spacer layers on either side of the DBQW, a drift layer on the collector side and contact layers on both sides as detailed in Table I. It was chosen in order to enhance the device *I-V* characteristics by maximising peak-to-valley voltage and current differences as proposed in [23].

TABLE I
RTD EPI-LAYER DESIGN

Layer	Thickness (Å)	Composition	Doping (cm^{-3})	Description
1	400	$In_{0.53}Ga_{0.47}As$	3E19 : Si	Collector
2	800	$In_{0.53}Ga_{0.47}As$	2E18 : Si	Sub-Collector
3	1200	$In_{0.53}Ga_{0.47}As$	5E16 : Si	Drift Region
4	100	$In_{0.53}Ga_{0.47}As$	2E16 : Si	Spacer
5	20	$In_{0.53}Ga_{0.47}As$	Un-doped	Spacer
6	25	AlAs	Un-doped	Barrier
7	47	$In_{0.53}Ga_{0.47}As$	Un-doped	Well
8	25	AlAs	Un-doped	Barrier
9	20	$In_{0.53}Ga_{0.47}As$	Un-doped	Spacer
10	100	$In_{0.53}Ga_{0.47}As$	2E16 : Si	Spacer
11	100	$In_{0.53}Ga_{0.47}As$	5E16 : Si	Spacer
12	800	$In_{0.53}Ga_{0.47}As$	2E18 : Si	Sub-Emitter
13	4000	$In_{0.53}Ga_{0.47}As$	3E19 : Si	Emitter
14	2000	InP	Un-doped	Buffer
		SI : InP		Substrate

RTD devices with 10 x 10 μm^2 top contact mesa were fabricated using optical lithography. Chemical wet etching (H_3PO_4:H_2O_2:H_2O = 1:1:38) was used to define the RTD mesa. This recipe has an etching rate of around 100 nm/min. Polyimide PI-2545 was used for device passivation. The Ohmic contacts comprised of Ti/Pd/Au (20/30/150 nm) metallization. The device contact resistance was characterized through TLM (transmission line method) measurements and found to be 2.6 Ω. The 20-Ω stabilising resistor was realised from a thin film NiCr (60:40) which has a sheet resistance of 50 Ω/square. It was realised across the coplanar wave-guide (CPW with 50 Ω characteristic impedance) input line and was 60 μm wide and 220 μm long. On the same sample, auxiliary test structures were fabricated with identical metal pads (CPW with length L = 220 μm) and resistor geometry (Fig. 2 bottom). A micrograph of the fabricated stabilized RTD and the auxiliary test structure is shown in Fig. 2.

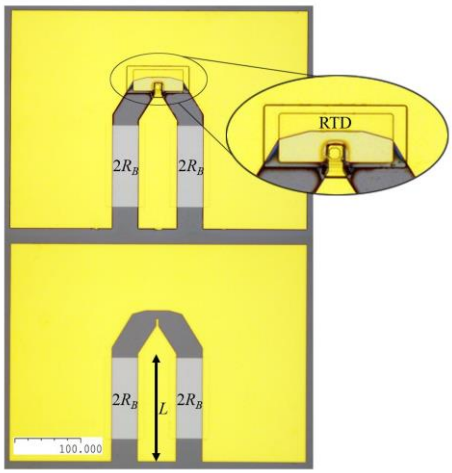

Fig. 2. Micrograph of a fabricated RTD with a 20 Ω stabilizing resistor (top) and de-embedding auxiliary test structure of pads and resistor (bottom).

The DC characterisation of the RTD was done using a Keysight B1500A device parameter analyser. The measured *I-V* characteristic of the stabilised device is presented in Fig. 3. The device exhibits a peak-valley bias voltage difference (ΔV) of around 2 V and peak-valley current difference (ΔI) of around 16 mA.

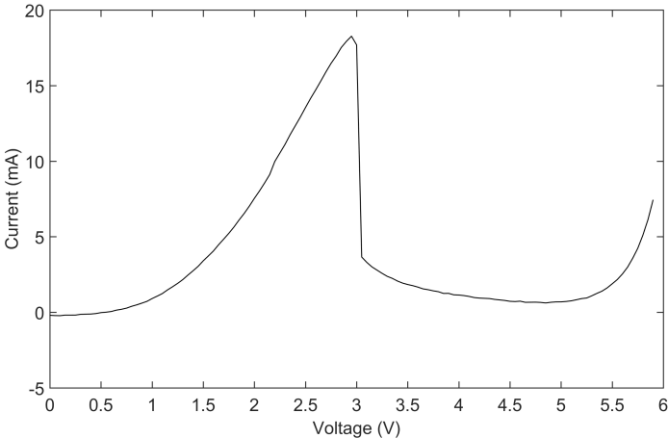

Fig. 3. Measured *I-V* characteristics of a stabilised RTD device.

IV. RF Device & Test-Fixture Characterisation

For S-parameter measurements, a Keysight E8361A vector network analyser (VNA) was used. The calibration was done using the short-open-load-through (SOLT) technique with a port power of -17 dBm. The frequency range was 10 MHz to 110 GHz.

To establish the applicability of the proposed de-embedding procedure, measurements of both a stabilized and an unstabilized device RTD device at identical bias points in the positive differential resistance (PDR) region were initially taken. The measured S_{11} parameters of a stabilised and un-stabilised RTD at a bias of at 2.9V (close to the peak region) are shown in Fig. 4.

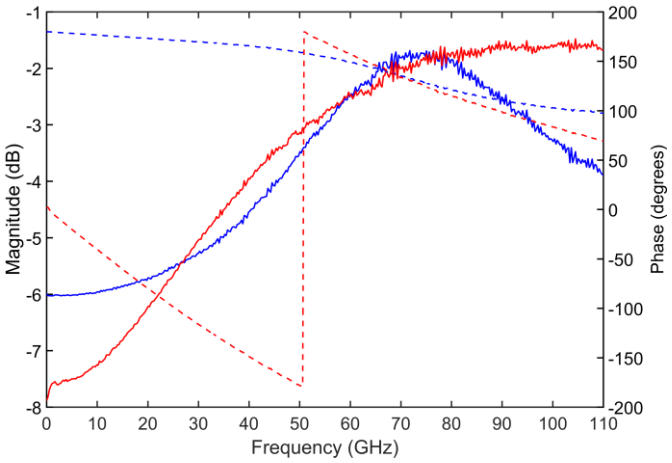

Fig. 4. S-parameters stabilised (blue trace) and unstabilised (red trace) RTD device biased at 2.9 V in the positive differential resistance (PDR) region – around the peak-current, showing magnitude (solid line) and phase (dashed line).

As expected, significant difference in acquired data can be observed across the frequencies for the stabilized device (blue curve), due to the presence of the shunt resistor. The proposed de-embedding method was applied in both cases using two-port measurements from their corresponding test structure (metal pads & shunt resistor – stabilised device; metal pads – un-stabilised device). Fig. 5. shows the S-parameters of the pads and shunt resistor test structure used for de-embedding the stabilised device. The de-embedded data is shown in Fig. 6. (blue trace) alongside that of the un-stabilised device (red trace). Good agreement can be observed between the two measurements under the same bias conditions, which validates the applicability of this procedure. There are some minor discrepancies, which can be attributed to the fabrication process not yielding two perfectly identical devices. Overall, this result shows that the proposed de-embedding method is not limited by a specific device external circuitry, and so is suitable to accommodate different bond-pad and stabilizing network configurations.

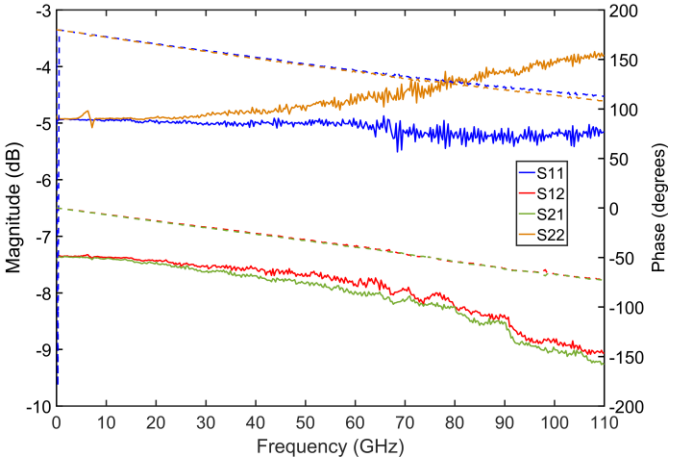

Fig. 5. S-parameters of the pads and shunt resistor test structure used for de-embedding the stabilised device.

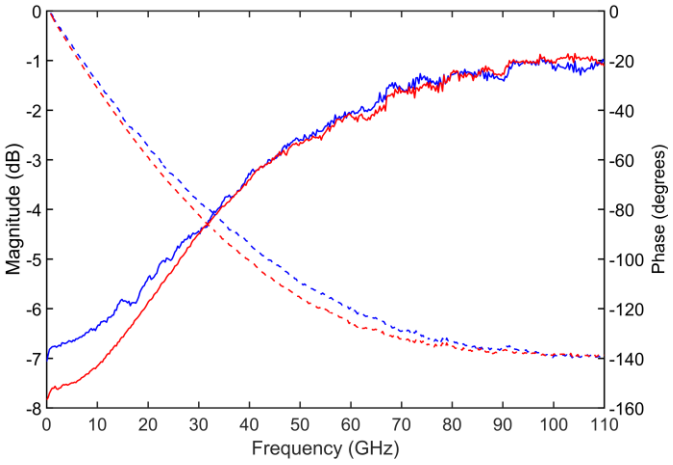

Fig. 6. S-parameters stabilised (blue trace) and unstabilised (red trace) RTD device biased at 2.9 V in the positive differential resistance (PDR) region, showing magnitude (solid line) and phase (dashed line) after the proposed de-embedding procedure.

V. Small-Signal Equivalent Circuit Modelling

Fig. 7. shows the small-signal equivalent circuit of an RTD [24]. It consists of a contact and access resistance R_s in series with the parallel combination of the device self-capacitance C_n together with the device conductance G_n which models the intrinsic current-voltage characteristic, and the quantum well inductance L_{qw} which models the charging and discharging effect of the quantum well.

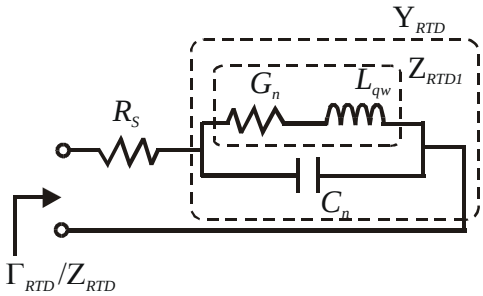

Fig. 7. Intrinsic small-signal equivalent circuit of an RTD. R_s is the contact and access resistance, G_n the device conductance, C_n the device self-capacitance and L_{qw} the quantum-well inductance.

An inspection of the circuit in Fig. 7. reveals that at high enough frequencies, C_n would provide a short-circuit path which would effectively mask any contributions to the input impedance from G_n and L_{qw}. This is clearer to see with a quasi-static model for the RTD, i.e. one which neglects L_{qw}. In this case, the impedance of the device can be written as:

$$Z_{RTD} = R_s + \frac{1}{G_n + j\omega C_n} = R_s + \frac{G_n - j\omega C_n}{G_n^2 + \omega^2 C_n^2}. \quad (3)$$

From (3), we can infer that the contact resistance R_s (which will typically be a few Ohms) dominates the real part of the device impedance at high frequencies, since G_n is typically a few milli-Siemens, C_n is tens of femtofarads or larger, and therefore the contribution of the intrinsic device to the device resistance can be negligible at millimeter-waves. Therefore, to determine the small-signal equivalent circuit elements of Fig. 7. the following procedure is proposed:

a) The de-embedded S-parameter data of the device (Γ_{RTD}) is first converted into Z-parameters which provides Z_{RTD}. A plot of the real part of Z_{RTD} with frequency at high frequency provides an estimate of R_s, i.e. $R_s \approx Re(Z_{RTD})_{\omega\to\infty}$.
Fig. 8. provides such plots for one bias point in the PDR and another in the NDR, respectively. As expected, the real parts of the input impedance become frequency independent at high frequencies, with $R_s \approx$ 2.5 Ω at V_{bias} = 1 V and $R_s \approx$ 3.5 Ω at V_{bias} = 3.1 V. These values of R_s are initial estimates at the respective bias voltages. The final value of R_s at each bias point is determined in conjunction with the simultaneous determination of the other intrinsic parameters, namely C_n, R_n and L_{qw}. Here, the basis of the parameter extraction is that each of these lumped elements is independent of frequency.

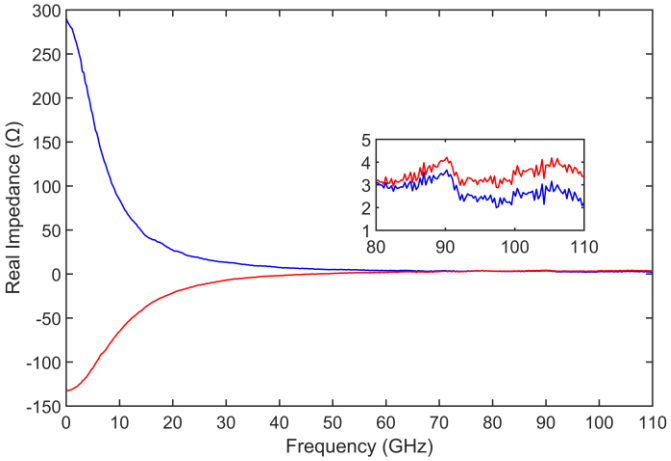

Fig. 8. Real part of Z-parameters in the PDR region at 1V (blue curve) and in the NDR region at 3.1V (red curve). The high frequency regions used for R_s estimation are presented in the inset graph.

Thus, the extraction of the equivalent circuit elements proceeds as follows:

b) We assume that R_s is known and de-embed it from Z_{RTD}. The resulting data then should represent C_n in parallel with G_n and L_{qw} and so can be concisely expressed using its admittance as follows:

$$Y_{RTD} = j\omega C_n + \frac{1}{R_n + j\omega L_{qw}} = \frac{R_n}{R_n^2 + \omega^2 L_{qw}^2} + j\omega\left(C_n - \frac{L_{qw}}{R_n^2 + \omega^2 L_{qw}^2}\right). \quad (4)$$

with $R_n = 1/G_n$.

c) From (4), it should be clear that a correct value of R_s would provide an imaginary part which varies linearly with frequency (at low frequencies). The value of R_s may be adjusted at this stage to achieve this. We can then estimate C_n using $C_n \approx Im(Y_{RTD})/\omega$ and de-embed it from the data. The resulting data then represents the series circuit of G_n and L_{qw}. As such, we can convert this data into an impedance which can be expressed as:

$$Z_{RTD1} = R_n + j\omega L_{qw}. \quad (5)$$

d) Using (5), a correct R_s (and C_n) should provide frequency independent values of R_n and L_{qw}. Thus, R_s and can be adjusted further to achieve this. In specific cases, for which the magnitude L_{qw} is large (i.e. in the NDR region), its effects can be observed more dominant at lower frequencies in the susceptance of the circuit ($Im(Y_{RTD})$). Using the estimation presented in (c) would provide an overcompensated value of C_n, which needs further adjustment in order to achieve linearity in the real and imaginary part of Z_{RTD1}.

In summary, starting with the estimate of R_s as described in step (a) above, the extraction of the other intrinsic RTD elements from measured data proceeds as described above. The

initial estimate of R_s may be varied within ±10% to achieve the expected frequency independence of C_n, R_n and L_{qw}. Example extraction results from the PDR and NDR regions of the RTD are shown in Fig. 9. and Fig. 10. respectively.

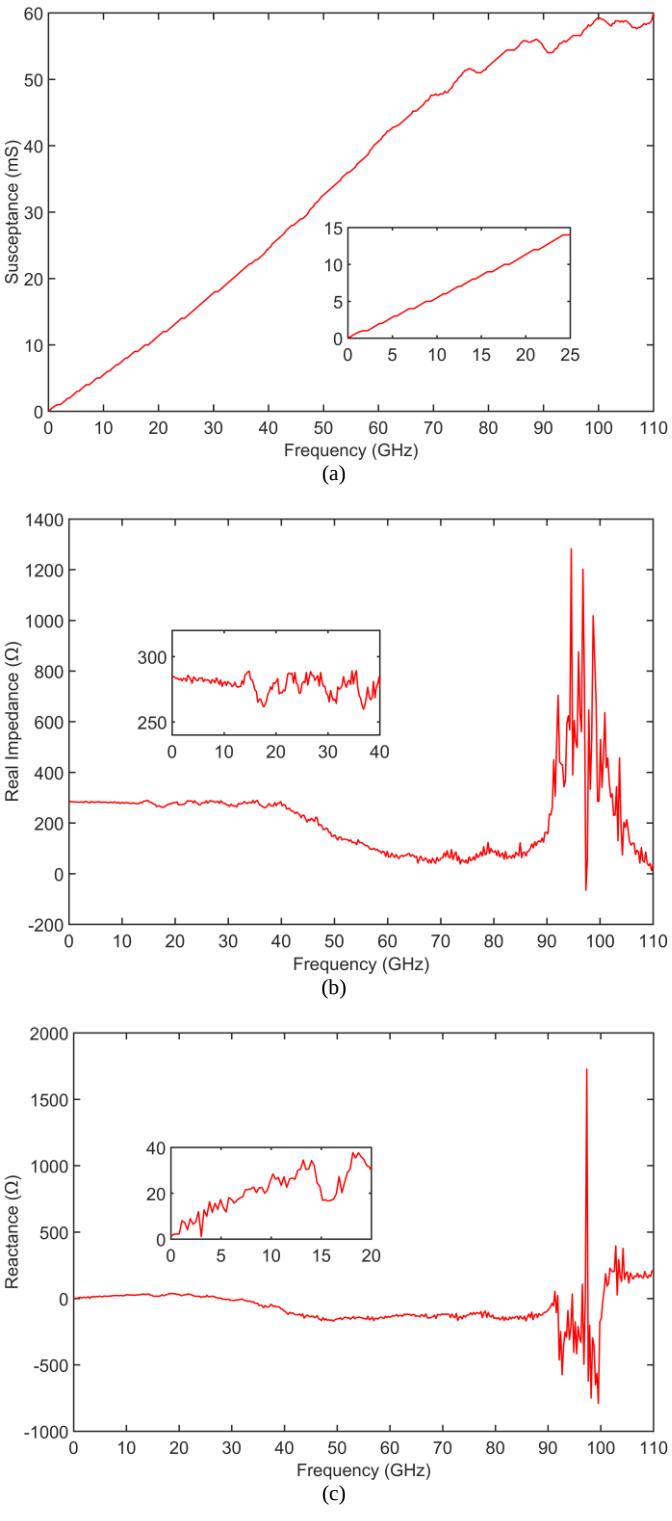

Fig. 9. Imaginary part of Y-parameters in the PDR region with de-embedded R_s – linear region shown in inset used to estimate C_n = 93 fF (a). Real part of Z-parameters in the PDR region with de-embedded R_s and C_n – linear region shown in inset used to estimate R_n= 284 Ω (b). Imaginary part of Z-parameters in the PDR region with de-embedded R_s and C_n – linear region shown in inset used to estimate L_{qw} = 0.37 nH (c).

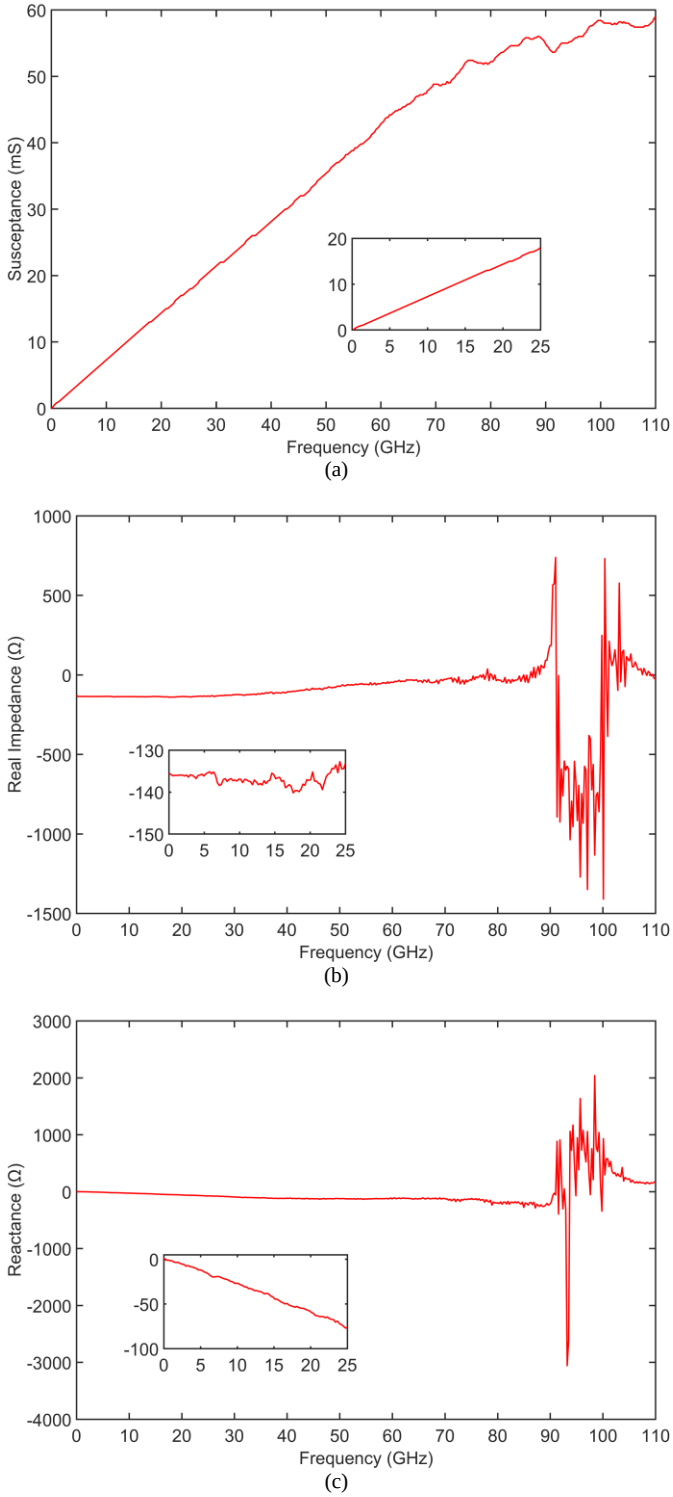

Fig. 10. Imaginary part of Y-parameters in the NDR region with de-embedded R_s – linear region shown in inset used to estimate C_n = 110 fF (a). Real part of Z-parameters in the NDR region with de-embedded R_s and C_n – linear region shown in inset used to estimate R_n = 136 Ω. Initial value of C_n adjusted to 94 fF to achieve linearity (b). Imaginary part of Z-parameters in the NDR region with de-embedded R_s and C_n – linear region shown in inset used to estimate L_{qw}= − 0.48 nH (c).

As may be seen from these graphs, the values of the intrinsic elements are largely independent of frequency at lower frequencies, up to around 40 GHz. Insets for the frequency bands used for the actual extraction are shown in each figure.

The somewhat random behaviour at higher frequencies may be attributed to reduced measurement accuracy at these frequencies.

The extracted parameters were used to compute simulated device input impedance and reflection coefficient. The results were compared with the measured data and are shown in Fig. 11. for the input impedance at two different bias points, one in the PDR and the other in the NDR. Fig. 12. shows the measured and simulated reflection coefficient for the NDR bias point on a Smith chart. Excellent agreement between measurement and simulated RTD data can be observed over the complete measurement frequency range, 10 MHz to 110 GHz, demonstrating the accuracy of the proposed procedure.

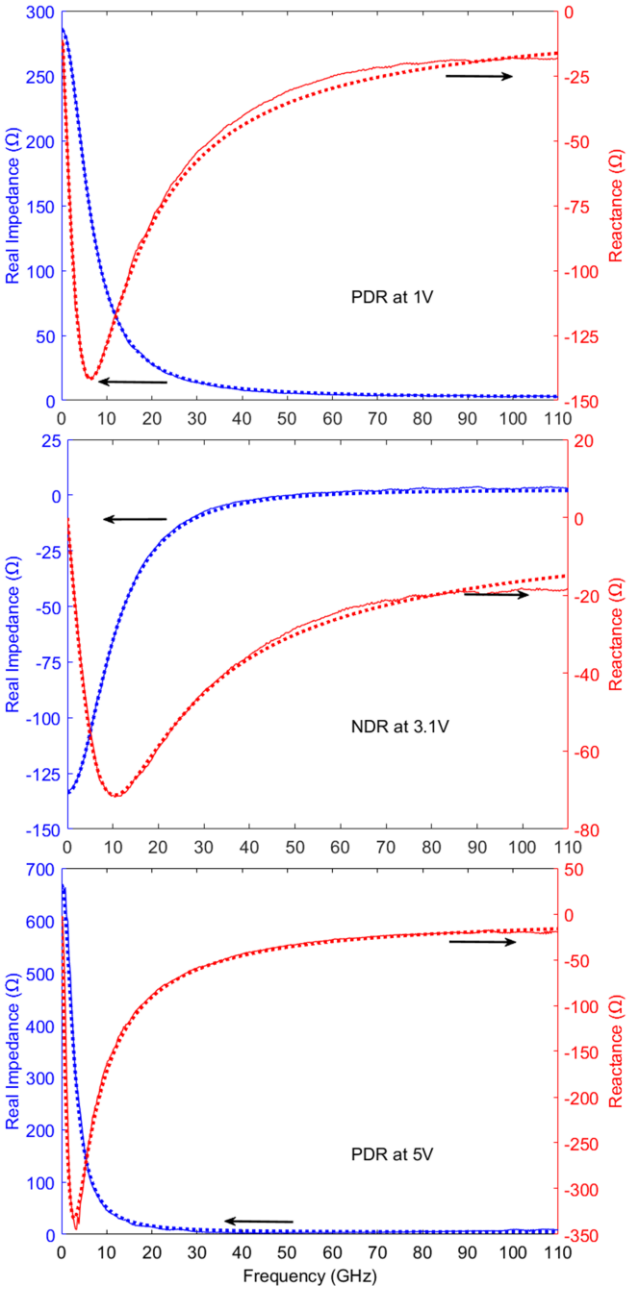

Fig. 11. De-embedded real and imaginary measured (line) and fitted (circles) Z-parameters of a stabilized RTD at 1V in the PDR region, at 3.1 V in the NDR region and at 5V in the post valley region.

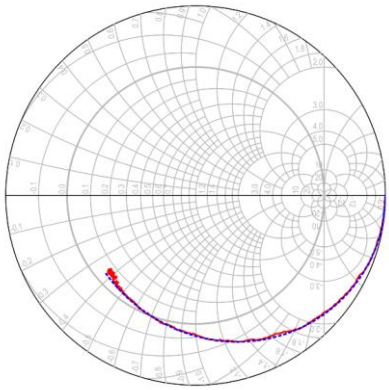

Fig. 12. De-embedded measured (red) and simulated (blue) S-parameter data of a stabilised RTD in the center of the NDR region (3.4 V).

Table II shows the extracted small-signal equivalent circuit elements at various bias points, throughout the entire bias range. In order to validate the accuracy of the extracted parameters a standard optimization process was further used, in order to obtain an error range for each coefficient (tabulated in brackets), with 95% confidence bounds.

TABLE II
PARAMETER EXTRACTION RESULTS

Bias Voltage (V)	R_s (Ω)	G_n (mS)	C_n (fF)	L_{qw} (nH)
1	2.5 (2.87)	3.52 (3.48 : 3.55)	93 (91 : 94)	0.37 (0.32 : 0.35)
2	3.18 (3.3)	11.11 (10.86 : 11.36)	86 (86 : 89)	0.11 (0.08 : 0.13)
2.9	3.5 (3)	7.57 (7.46 : 7.75)	85 (84 : 89)	0.17 (0.15 : 0.2)
3.1	3.6 (3.9)	-7.35 (-7.46 : -7.35)	94 (91 : 95)	-0.478 (-0.54 : -0.45)
3.4	3.73 (3.9)	-3.83 (-3.83 : -3.76)	92 (92 : 93)	-0.63 (-0.62 : -0.6)
3.6	3.8 (4)	-2.52 (-2.56 : -2.51)	91 (88 : 91)	-0.80 (-0.88 : -0.79)
4.8	4.3 (4.23)	0.52 (0.5 : 0.53)	90 (87 : 91)	8 (8.12 : 8.5)
5	4.42 (4)	1.49 (1.49 : 1.51)	90 (86 : 90)	1.8 (1.78 : 1.89)
5.2	5.12 (5.12)	3.09 (3.07 : 3.09)	89 (87 : 90)	0.54 (0.54 : 0.56)
5.4	5.23 (4.87)	5.2 (5.15 : 5.23)	88 (86 : 91.5)	0.28 (0.27 : 0.29)

The results of the complete extraction procedure indicate a relatively small linear bias dependence of the contact and access resistance R_s (1.3 Ω over a range of 4V) This variation was possible to observe due to the high frequency nature of the S-parameter measurements (between 80 – 110 GHz), as it is generally compensated at lower frequencies by errors in the extracted values of device conductance G_n. We think that this phenomenon could be related to the electric field dependence of the carrier mobility [25], and will be investigated further.

VI. OTHER ESTIMATION TECHNIQUES FOR RTD ELEMENTS

This section reviews previously used methods to estimate the RTD small-signal equivalent circuit elements and compares

these with the new approach described in the preceding section. In particular, physics-based approaches for estimating C_n and L_{qw} are described, but first the alternative techniques of determining R_s and G_n are described.

A. Device contact resistance and differential conductance

The metal-semiconductor contact resistance can be determined experimentally by using standard transmission line model (TLM) measurements. For the devices described in this paper, the estimated R_s is ~2.6 Ω for the 10 μm × 10 μm RTDs. This contact resistance can be de-embedded from the measured *I-V* characteristics (Fig. 3) to yield the intrinsic device *I-V* characteristics. The differential conductance G_n can be computed directly from these characteristics. Good agreement can be seen in Fig. 13. between the variation of G_n with bias and extracted G_n values from S-parameter data.

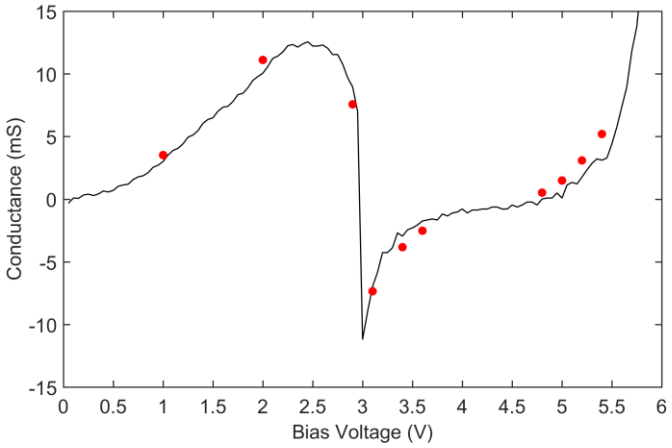

Fig. 13. Differential device conductance G_n computed from the intrinsic *I-V* characteristics (black trace) and extracted (red dots).

B. Device capacitance

The RTD self-capacitance (C_n) comprises the device geometric capacitance (C_0) and the quantum-well capacitance (C_{qw}), which arises from the electron density change in the quantum well as a function of applied bias, and so is given by:

$$C_n = C_0 + C_{qw}. \tag{6}$$

Considering the DBQW structure as a standard parallel-plate capacitor (an undoped region confined between a highly doped collector and emitter), C_0 can be approximated by:

$$C_0 = \frac{A}{\frac{L_w}{\epsilon_w}+\frac{2L_b}{\epsilon_b}+\frac{L_d}{\epsilon_d}}. \tag{7}$$

where L_w, L_b, L_d, are the widths of the quantum well, barrier and depletion region (4.7 nm 2.5 nm, 120 nm) and ε_w, ε_b, ε_d, are the corresponding material dielectric constants (13.1, 13.1 [26], 10.1 [27]). This equates to 88 fF for the presented epi-layer structure. The extracted device capacitance from S-parameters, which corresponds to C_n, indicates that the static capacitance C_0 is slightly higher (~90 fF). Thus, C_{qw} can be determined from the total capacitance variation using (6).

The basis of the charge variation has been derived by [28] and validated in [16], and can be described by the change in quantum-well – collector current density (J_c) as a function of electron escape ν_c (s^{-1}), and thus C_{qw} is also expressed as:

$$C_{qw} = A\frac{\Delta Q_c}{\Delta V} = -\frac{G_n}{\nu_c}. \tag{8}$$

where ΔQ_c represents the variation of charge in the collector, $\Delta Q_c \approx -\Delta Q_{qw}$ assuming no contribution from the electrons tunneling back from the quantum-well into the emitter. Therefore using (6)-(8), i.e. C_n and extracted G_n, ν_c can be determined. It can be seen that quantum well-collector escape rate (assumed bias independent) is $1/\nu_c \approx 0.55$ ps. From this value and the differential conductance in Fig. 13. the modelled capacitance variation with bias is plotted in Fig. 14. alongside the extracted device capacitance from the S-parameter data.

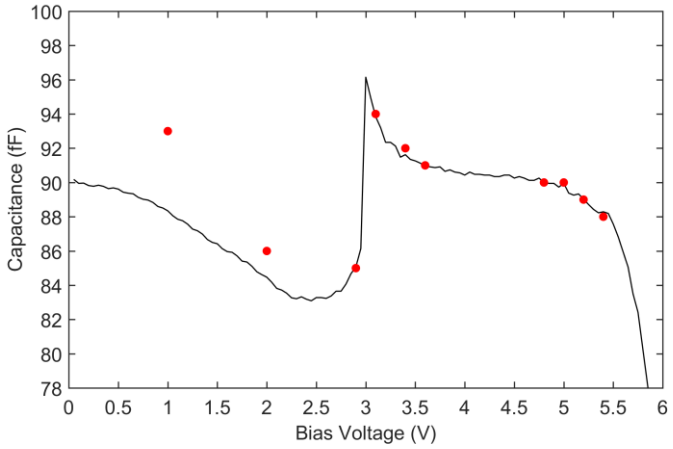

Fig. 14. RTD Device capacitance C_n simulated (black trace) and extracted (red dots).

C. Quantum well inductance

As earlier described, the quantum-well inductance (L_{qw}) is attributed to the charging and discharging effect of the quantum-well, and is given by [24]:

$$L_{qw} = \frac{\tau_{dwell}}{G_n}. \tag{9}$$

where τ_{dwell} is the electron quasibound-state lifetime in the quantum-well [29] and can be estimated from:

$$\tau_{dwell} = \frac{\hbar}{\Delta E_n}. \tag{10}$$

Here, ΔE_n is the energy full-width of the transmission probability function through the resonant state which can be obtained by the Wentzel–Kramers–Brillouin (WKB) approximation method as follows:

$$\Delta E_n = E_n \exp\left[-2L_b\sqrt{\frac{2m_b(U_0-E_n)}{\hbar^2}}\right]. \tag{11}$$

E_n is the nth resonance level, L_b is the width of the barrier (2.5 nm), U_0 is the barrier energy level (1.322 eV) and m_b is the

effective electron mass in the barrier. Fig. 15 shows the transmission probability through the RTDs DBQW structure using WinGreen software, which is a nonequilibrium Green function based 1D quantum transport simulator [30]. The estimation for the carrier lifetime is generally calculated for the first resonance energy level (E_0 = 0.17 eV for this structure), however, the transmission probability plot suggests that the primary resonant current occurs at a higher energy level (E_1 = 0.73 eV).

Using (10) and (11), the computed value for τ_{dwell} was calculated to be 1.86 ps, and then using (9) and the intrinsic G_n (Fig. 7), the variation of L_{qw} with bias was calculated and is shown in Fig. 16. (black solid trace). As expected, the computed inductance becomes negative in the NDR region following the nature of the differential conductance.

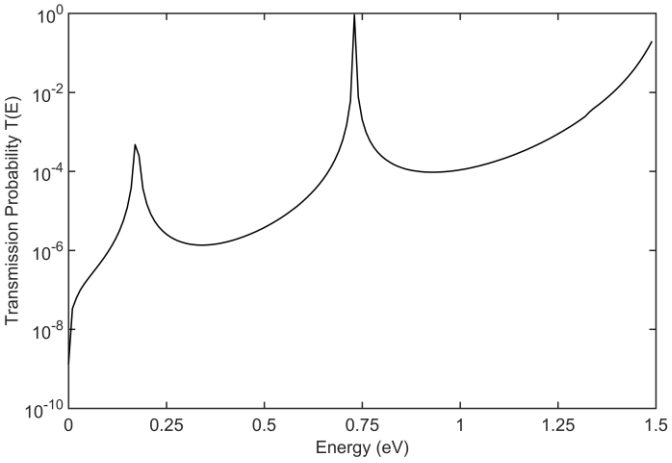

Fig. 15. WinGreen [30] simulation of the transmission probability for the measured RTD layer structure.

The extracted values of L_{qw} from S-parameter data are also shown in Fig. 16 (red dots), and good agreement between simulated and extracted values can be seen.

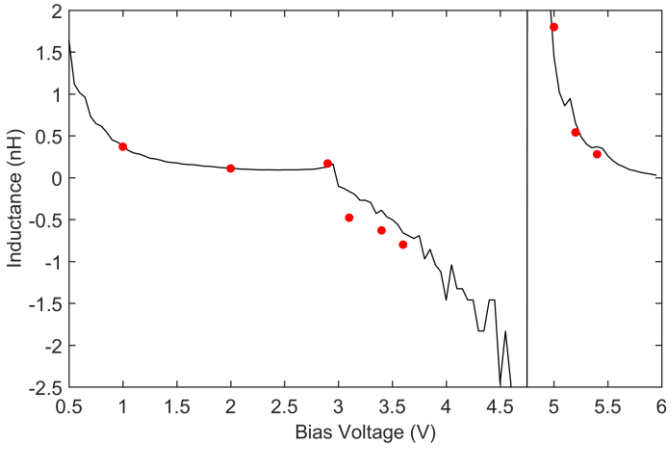

Fig. 16. Quantum-well inductance L_{qw}: simulated (black trace) and extracted (red dots).

Finally, using (9) and the extracted values of L_{qw} and G_n the electron lifetime τ_{dwell} from S-parameter data is approx. 1.15 ps, which is in fair agreement with the theoretical value of 1.86 ps. From Fig. 16, it can be seen that the largest discrepancy between the simulated and experimentally extracted electron life time can be observed around the centre of the NDR region. This effect can be simply explained by the variations of the electron escape rates through the barriers, which were assumed bias independent throughout simulations.

VII. Conclusion

A universal on-wafer bond-pad and shunt resistor de-embedding technique for stabilised RTDs was proposed and demonstrated up to 110 GHz for a 10 x 10 μm^2 InP RTD device. The accuracy of the method relies principally on measured data from one test structure. Further, a new simple and robust small-signal equivalent circuit parameter extraction procedure for RTDs which yielded physically relevant parameters and provided an excellent fit between the model and measured S-parameter data up to 110 GHz was described. It is expected that these results will accelerate the development of RTD technology for THz applications by providing the foundation to develop compact CAD models for the device.

Acknowledgments

The authors would like to extend their thanks to the James Watt Nanofabrication Centre (JWNC) staff, at the University of Glasgow, for their support in the device fabrication, and also the support of the European Regional Development Fund (FEDER), Competitiveness and Internationalization Operational Programme (Compete 2020) of the Portugal 2020 framework RETIOT project (POCI-01-0145-FEDER-016432).

References

[1] I. Hosako, N. Sekine, M. Patrashin, S. Saito, K. Fukunaga, Y. Kasai, P. Baron, T. Seta, J. Mendrok, S. Ochiai and H. Yasuda, "At the dawn of a new era in terahertz technology," *Proc. IEEE*, vol. 95, no. 8, pp. 1611-1623, 2007

[2] N. Orihashi, S. Suzuki, and M. Asada, "One THz harmonic oscillation of resonant tunneling diodes," *Appl. Phys. Lett*., vol. 87, no. 23, Dec. 2005

[3] M. Asada, S. Suzuki, and N. Kishimoto, "Resonant tunneling diodes for sub-terahertz and terahertz oscillators," *Jpn. J. Appl. Phys*., vol. 47, no. 6R, pp. 4375, Jun. 2008

[4] S. Suzuki, M. Asada, A. Teranishi, H. Sugiyama, and H. Yokoyama, "Fundamental oscillation of resonant tunneling diodes above 1 THz at room temperature," *Appl. Phys. Lett*., vol. 97, no. 24, Dec. 2010

[5] A. Al-Khalidi, J. Wang and E. Wasige, "Compact J-band oscillators with 1 mW RF output power and over 110 GHz modulation bandwidth," *43nd Int. Conf. on Infrared, Millimeter, and Terahertz Waves (IRMMW-THz)*, 2018.

[6] R. Izumi, S. Suzuki and M. Asada, "1.98 THz Resonant-tunneling-diode oscillator with reduced conduction loss by thick antenna electrode," *42nd Int. Conf. on Infrared, Millimeter, and Terahertz Waves (IRMMW-THz)*, pp. 1-2, 2017.

[7] H.-J. Song and T. Nagatsuma, *Handbook of Terahertz Technologies: Devices and Applications*. Boca Raton, FL, USA: CRC Press, Apr. 2015.

[8] N. Oshima, K. Hashimoto, S. Suzuki, and M. Asada, "Wireless data transmission of 34 Gbit/s at a 500-GHz range using resonant-tunnelling-diode terahertz oscillator," *Electron. Lett.*, vol. 52, no. 22, pp. 1897-1898, 2016.

[9] J. Wang, A. Al-Khalidi, L. Wang, R. Morariu, A. Ofiare and E. Wasige, "15 Gbps 50 cm Wireless link using a high power compact III-V 84 GHz transmitter," *IEEE Trans. Microw. Theory Techn.*, vol. 66, no. 11, pp. 4698-4705, Nov. 2018.

[10] N. Nishigami, Y. Nishida, S. Diebold, J. Kim, M. Fujita, and T. Nagatsuma, "Resonant tunneling diode receiver for coherent terahertz

wireless communications," *Proc. Of 2018 Asia-Pacific Microw. Conf.,* pp. 726-728, 2018.
[11] T. Miyamoto, A. Yamaguchi, and T. Mukai, "Terahertz imaging system with resonant tunneling diodes," *Jpn. J. Appl. Phys*. vol. 55, 2016
[12] C. Kidner, I. Mehdi, J. R. East, and G. I. Haddad, "Bias circuit instabilities and their effect on the dc current-voltage characteristics of double-barrier resonant tunneling diodes," *Solid State Electron.*, vol. 34, no. 2, pp. 149-156, 1991.
[13] M. Reddy *et al*., "Bias stabilisation for resonant tunnel diode oscillators," *IEEE Microw. Wirel. Compon. Lett.*, vol. 5, no.7, pp. 219-221, 1995.
[14] J. T. Wallmark and A. H. Dansky, "Nonlinear biasing resistors for microwave tunnel-diode oscillators*," IEEE Trans. Microw. Theory Techn.*, pp. 260-262, vol. 11, 1963.
[15] L. Wang, J. M. L. Figueiredo, C. N. Ironside, and E. Wasige, "DC Characterization of tunnel diodes under stable non-oscillatory circuit condition", *IEEE Trans. Electron Devices*, vol. 58, no. 2, pp. 343-347, 2011.
[16] Q. Liu, A. Seabaugh, P. Chamhal, F.J. Morris, "Unified AC model for the resonant tunneling diode", *IEEE Trans. Electron Devices*, vol. 51, no. 5, pp. 653-657, May 2004.
[17] C. Kidner, I. Mehdi, J.R. East and G.I. Haddad, "Power and stability limitations of resonant tunneling diodes," *IEEE Trans. Microw. Theory Techn.*, vol. 38, no. 7, pp. 864-872, 1990.
[18] T. Wei, S. Stapleton, and O. Berolo, "Scattering parameter measurements of resonant tunneling diodes up to 40 GHz," *IEEE Trans. Electron Devices*, vol. 42, no. 7, pp. 1378-1380, Jul. 1995.
[19] A. Teranishi et al., "Fundamental oscillation up to 1.08 THz in resonant tunneling diodes with high-indium-composition transit layers for reduction of transit delay," *IEICE Electron. Exp.*, vol. 9, no. 5, pp. 385-390, Mar. 2012
[20] S. G. Muttlak, O. S. Abdulwahid, J. Sexton, M. J. Kelly and M. Missous, "InGaAs/AlAs Resonant Tunneling Diodes for THz Applications: An Experimental Investigation," *IEEE J. Electron Devices Soc.*, vol. 6, pp. 254-262, 2018.
[21] S. Diebold, S. Nakai, K. Nisio, J. Kim, K. Tsuruda, T. Mukai, M. Fujita and T. Nagatsuma, "Modeling and simulation of terahertz resonant tunneling diode-based circuits," *IEEE Trans. THz Sci. Technol.*, vol. 6, no. 5, September 2016.
[22] G. Gonzalez, "Microwave transistor amplifiers: analysis and design", *Pearson*, 2nd edition, 1996.
[23] S. Javalagi, V. Reddy, K. Gullapalli, D. Neikirk, "High efficient microwave diode oscillators", *Electron. Lett.*, vol. 28, pp. 1969-701, 1992.
[24] E.R. Brown, C.D. Parker, T.C.L.G. Sollner, "Effect of quasibound-state lifetime on the oscillation power of resonant tunneling diodes", *Appl. Phys. Lett.*, vol. 54, pp. 934-936, Mar. 1989.
[25] C. Nasser, D. Ritter, and M. Rudolph, "Bias dependence of the access resistance in GaN HEMTs," *Proc. 22nd Int. Microw. Radar Conf. (MIKON)*, pp. 271-273, May 2018.
[26] P. Bhattacharya, ed., "Properties of Lattice-Matched and Strained Indium Gallium Arsenide," *EMIS Datareviews Series, IEE INSPEC*, no. 8, 1993.
[27] S. Tiwari, "Compound Semiconductor Device Physics". *Academic Press*, 1992.
[28] R. Lake and J. Yang, "A physics based model for the RTD quantum capacitance," *IEEE Trans. Electron Devices*, vol. 50, no. 3, pp. 785-789, Mar. 2003.
[29] T.C.LG. Sollner, E.R. Brown, W.D. Goodhue, and H.Q. Le, "Observation of millimeter-wave oscillations from resonant tunneling diodes and some theoretical considerations of ultimate frequency limits", *Appl. Phys. Lett*., vol. 50, pp. 332-334, 1987.
[30] https://www.hs-rm.de/en/rheinmain-university/people/indlekofer-klaus-michael/research-and-development/wingreen/

Razvan Morariu received the M.Eng. degree in Electronics and Electrical Engineering in 2016 from the University of Glasgow, Glasgow, U.K., where he is currently working towards the Ph.D. degree in the design and characterization of RTD-based terahertz oscillators and detectors.

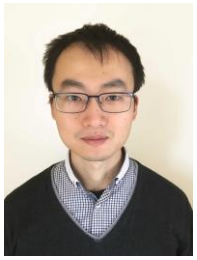

Jue Wang received the PhD degree in Electronics and Electrical Engineering from the University of Glasgow in 2014. From 2014 until now, he has been working on resonant tunneling diode-based terahertz oscillator design as a postdoctoral researcher. His current research interests include high power terahertz devices and terahertz applications including wireless communications, imaging, etc.

Andrei Catalin Cornescu received the BEng. degree in Electronics and Electrical Engineering in 2015 from the University of Glasgow, Glasgow, U.K., where he is currently working towards the Ph.D. degree in the design and characterization of resonant tunneling diode (RTD)-based terahertz oscillators and detectors.

Abdullah Al-Khalidi received his BEng, MSc and PhD degrees from the University of Glasgow in 2010, 2011 and 2015, respectively. He is currently working as a postdoctoral researcher at the University of Glasgow. His main research interest is in THz resonant tunnelling diodes (RTDs) and gallium nitride (GaN) transistor technologies.

Afesomeh Ofiare received the BEng degree in Electrical and Electronic Engineering from Madonna University, Nigeria in 2005, and received the MSc and Ph.D. degrees in Electronic and Electrical Engineering from the University of Glasgow, UK in 2009 and 2016 respectively. He is currently a Research Assistant at the University of Glasgow. His present research interests include high-frequency device characterisation, antennas for millimetre-wave and THz applications and wireless communications.

José M. L. Figueiredo (M'09) received the B.Sc. degree in Physics and the M.Sc. degree in Optoelectronics and Lasers from the University of Porto, Portugal, in 1991 and 1995, respectively, and the Ph.D. degree in Physics from the University of Porto in "co-tutela" with the University of Glasgow, Glasgow, U.K., in 2000. He worked with the University of Glasgow on the optoelectronic properties of resonant tunneling diodes. He is with the Department of Physics, Faculty of Sciences of the University of Lisbon. His current research interests include applications of resonant tunneling diodes and resonant tunneling diode based optoelectronic devices, and neural-inspired photonic circuits.

Edward Wasige (S'97, M'01) received the BSc. (Eng.) degree in Electrical Engineering from the University of Nairobi, Kenya, in 1988, the MSc.(Eng.) from the University of Liverpool (UK) in 1990, and the PhD degree in Electrical Engineering from Kassel University (Germany) in 1999. Prior to becoming a Lecturer at the University of Glasgow in 2002, he was a UNESCO postdoctoral fellow at the Technion – Israel Institute of Technology and before that a Lecturer at Moi University (Kenya). His current research interests include compound semiconductor micro/nanoelectronics and applications with focus on GaN electronics and RTD-based terahertz electronics.